

# A Quadrotor with a Passively Reconfigurable Airframe for Hybrid Terrestrial Locomotion

Huaiyuan Jia, Songnan Bai, Runze Ding, Jing Shu, Yanlin Deng,  
Bee Luan Khoo, and Pakpong Chirarattananon, *Member, IEEE*

**Abstract**—Despite efforts to circumvent and alleviate the impact of a mid-flight collision, it remains extremely challenging to safeguard a multirotor vehicle when it operates in cluttered environments. In this work, we introduce a flying robot with the ability to roll through a gap narrower than its diameter to prevent a possible aerial collision entirely. The novelty of the proposed design lies in a simple passive mechanism that redirects the propelling thrust for the terrestrial operation without the need for extra actuators. As a result, the robot remains compact and lightweight. Furthermore, to overcome the underactuation associated with the passive structure, the transitions between flight and rolling are accomplished with a highly dynamic maneuver. In the experimental demonstration, the robot seamlessly switched between the aerial and terrestrial locomotion to safely negotiate a 10-cm opening.

**Index Terms**—aerial robots, passive mechanisms, collision avoidance, multimodal locomotion.

## I. INTRODUCTION

SIGNIFICANT progress in localization and planning [1], [2], design and mechanisms [3], aerial swarms [4], etc., has accelerated the deployment of Micro Aerial Vehicles (MAVs) for several applications, including transportation of payload [5]–[7], search and rescue [8], and aerial manipulation [9]. With the surge of real-world usage, these flying robots are anticipated to operate in increasingly challenging environments and may be subject to wind disturbances [10]. As a result, several strategies have been followed to let these small robots safely negotiate and pass through cluttered environments.

Among these, there exist navigation-based methods that directly [11], [12] and indirectly [13] emphasize on obstacle detection and planning for collision avoidance. Such frameworks oftentimes rely substantially on estimation, sensing, and computation for robots to evade any physical obstructions. In the view that an accidental collision is inevitable, one emerging research avenue is the development of impact-resilient vehicles [14]–[16]. One pioneering solution is the integration of a protective frame capable of mitigating the impulse from an impact [17]–[20]. The concept has evolved into origami airframes that soften upon encountering an impact, preventing a possible structural damage from an in-flight crash or a subsequent fall [21], [22]. The built-in feature

This work was supported by the Research Grants Council of the Hong Kong Special Administrative Region of China (grant number CityU 11205419).

H.J., S.B., R.D., Y.D., B.L.K., and P.C. are with the Department of Biomedical Engineering, City University of Hong Kong, Hong Kong SAR, China (emails: hhjia2-c@my.cityu.edu.hk, pakpong.c@cityu.edu.hk). J.S. is with the Department of Biomedical Engineering, Chinese University of Hong Kong, Hong Kong SAR, China.

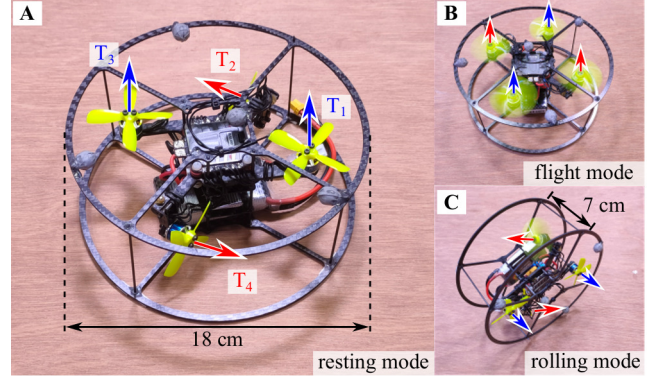


Fig. 1. Configurations of the bimodal quadrotor with two passive revolute joints. Blue arrows indicate the axes of the fixed propellers ( $T_1$  and  $T_3$ ) and red arrows indicate the axes of the pivoted propellers ( $T_2$  and  $T_4$ ). (A) The robot in the default state. (B) Two passive joints are activated for flight by the propelling thrusts when they are driven at high motor commands. (C) The vehicle in the rolling configuration produces the rolling thrust by the two tilted propellers in their default configuration. In this case, the passive joints are not activated due to the low propelling forces. The width of the robot in the rolling mode is narrower than that of the flight mode.

eliminates the need for outer protective shells, shrinking the footprint of the vehicles, which simultaneously reduces the risk of collisions.

More recently, the use of mechanical design and compliant mechanisms [23], [24] to facilitate the collision avoidance has been introduced in the form of transformable vehicles, a morphing quadrotor with a single servomotor was proposed to allow the robot to fold the structure and reduce its span for negotiating narrow apertures [25]. A similar principle was adopted in [26], with four servomotors that separately govern the configuration of four propellers. This brings about several possible vehicular configurations depending on the required operating scenarios. Another deformable vehicle, also with four servomotors, makes use of scissor-like elements instead of simple folds to accomplish the radial adjustment of the airframe to let it fly through a small opening [27]. In another implementation, the multi-link transformable robot in [20] is able to go through a small passage using a snake-like maneuver by leveraging its multiple structural degrees of freedom. A servomotor was integrated into each link to realize the transformation. It can be seen that, these flying robots achieve mid-air reconfigurability via the use of additional actuators or servomotors. The use for extra actuators, however, is detrimental to flight endurance and payload capacity. This motivates the passive morphing design in [28]. Therein, the

robot shrinks its footprint through passive joints when the propelling commands are temporarily lowered, allowing the vehicle to exploit its built-up momentum to squeeze through a narrow gap.

In this article, we propose an alternative approach for an aerial vehicle to deal with tight spaces. To eliminate the possibility of a collision and subsequent damages in a narrow passage, the robot lands and safely travels through the gap via rolling before resuming its flight, re-purposing the protective cage as a wheel to realize the rolling motion as demonstrated in Video S1. The strategy benefits from the reduced span of the vehicle in its terrestrial mode of locomotion as depicted in Fig. 1. Moreover, the entire process is accomplished through a passively morphing airframe, eliminating the need for additional actuators and increased power consumption.

As displayed in Fig. 1A, by default, two propellers on the proposed robot are horizontally directed. When spinning at high speeds, the produced thrust induces a rotation about the compliant revolute joint, re-orienting the thrust vector upwards for flight (Fig. 1B). On the other hand, in the rolling configuration (Fig. 1C), the tilted propellers directly provide the rolling torque without activating the passive joints as they are driven at lower speed.

There exist several aerial robots capable of ground operations, either via the use of wheeled [29]–[32] or legged [33]–[37] locomotion. While multi-legged configurations are more suitable for irregular or challenging terrains [35], wheeled locomotion benefits from its speed and efficiency [38], rendering it attractive as a secondary mode of locomotion for flying robots due to the high energetic requirements of flight. Furthermore, compared to most aerial vehicles capable of terrestrial locomotion, the proposed design possesses two advantages. First, the use of passive joints eliminates the need for extra actuators or servo motors for the transformation or operation as present in [32], [33], [35]–[37]. As a result, the flight endurance is minimally affected. Second, the proposed robot's design in this work has an advantage of reduced width when it operates in terrestrial mode, thanks to its unique rolling configuration as seen in Fig. 1C. With the width of only 7 cm in the rolling state, the robot is capable of passing through a gap as narrow as 10 cm. This cannot be achieved with other small multirotor vehicles. For instance, the prevalent 30-gram Crazyflie (Bitcraze) platform has the shortest distance between two propeller tips of 11 cm. To this end, the rolling mode renders the robot well suited for search and rescue missions or cluttered environments. On the other hand, another multirotor vehicle with a wheel-like rolling mode in [39] features a similar narrow body in the terrestrial operation via the incorporation of variable-pitch propellers. Nevertheless, the sophisticated mechanism and extra actuators associated with it are unsuitable for smaller robots. In this work, the need for such components is substituted by the passively transformable airframe.

Despite the mentioned benefits, the proposed design with the passive transformation makes the transition between the two operating modes a challenging task. As it can be deduced from Fig. 1A, an actuation of one of the upright propellers would generate torque to re-orient the robot towards the mono-

wheel configuration as desired. However, in the rolling mode (Fig. 1C), the robot is unable to directly take off. To overcome this, we devised a dynamic maneuver by taking advantage of the nonlinearity of the rotation groups. The rotation in the non-actuated direction is accomplished through simultaneous perpendicular rotations about two other axes (rolling and turning). Starting from rolling, an impulse torque is generated to sharply induce a turn at a suitable moment in the desired direction. As a result, the transition to the flight mode is reliably accomplished without requiring extra actuators. The outcome illustrates how a specifically designed dynamic maneuver can be leveraged to resolve the underactuated nature of the robot.

In the next section, the design of the vehicle and the analysis of the passively reconfigurable airframe is provided, including the requirements for bimodal operations. Section III describes the dynamics and control of the quadrotor in the flight and rolling stages, as well as the strategy for transitioning between them. The fabrication of the prototype is detailed in Section IV. The experimental results demonstrating the flight and transitions of the multimodal quadrotor are presented and discussed in Section V. This highlights the scenario in which the robot rolled through a tight gap in between the flights to refrain from a collision. Lastly, a conclusion is provided in Section VI.

## II. ROBOT DESIGN AND PASSIVE RECONFIGURATION

Herein, the overview of the robot's design is first discussed, followed by the working principles of the morphing airframe.

### A. Design Overview

One goal of the vehicle design is to allow the platform not only to fly, but also to roll through narrow apertures during its mission. To enable the robot to negotiate narrow gaps in the *rolling* mode, we take advantage of the thin disc-like profile of conventional multirotor vehicles. The proposed robot, shown in Fig. 2A with the body-fixed frame  $\mathcal{B} = \{X_B, Y_B, Z_B\}$ , is capable of rolling through a gap smaller than its original footprint by adopting a protective frame that also functions as a wheel. Unlike other rolling cage designs [29]–[31], the proposed robot is oriented differently from the flight stage. The resultant wheel-like configuration makes the platform much narrower (7 cm) compared to its flight configuration (18 cm). The rolling-to-flying width ratio of 7:18 or 0.39 is much lower than the 1:1 ratio of previous rolling quadcopters [31].

To generate the rolling torque about the original yaw axis ( $Z_B$ ), two propellers are attached to the airframe via passive revolute joints, allowing the force direction to change according to the operating mode without extra actuators. As schematically depicted in Fig. 2A, two compliant joints with the axes of rotation parallel to the  $Y_B$  axis are incorporated on the airframe. In the *resting* (Fig. 1A) and *rolling* (Fig. 1C) configurations, rotors 2 and 4 are either lightly or not actuated, the propeller axes remains approximately perpendicular to  $Z_B$ . When rolling, the generated thrust induces yaw torque (about  $Z_B$ ) and results in an efficient rolling motion of the robot

(when compared with the use of rotor-induced drag torque from rotors 1 and 3).

With sufficiently large actuation, the torque induced by the propeller's thrust about the revolute joint overcomes the joint's compliance. The joints associated with rotors 2 and 4 rotate to the maximum limit of  $90^\circ$ , forming a configuration identical to a conventional quadrotor. In this *flight* mode, the robot behaves as a regular multirotor robot, requiring no additional operational considerations.

### B. Passive Joint Design

*1) Design Principle:* The compliant joint is the key enabler of the multi-modal capability. As shown in Fig. 2A, the joint design is abstracted as links, stoppers, and an elastic component. This design adopts the elastic component to generate a nonlinear restoring torque. The nonlinear response and joint stoppers ensure that the propeller axis stays perpendicular to  $Z_B$  when it is lightly actuated for rolling and becomes aligned with  $Z_B$  for flying when the propeller thrust is sufficiently large.

The proposed joint design is shown in Fig. 2A. Link 1 is fixed against the airframe, serving as a mechanical ground. Link 2 is connected to Link 1 via a free revolute joint with a motor and propeller pair mounted at the tip. An elastic element couples these two links to create nonlinear restoring torque. Joint stoppers are adopted to limit the range of motion.

Compared to a servo-actuated mechanism, the linkage-based design reduces the vehicle's mass and power, benefiting for the flight endurance. Simultaneously, the strategy makes use of revolute joints and spring-like components. This facilitates the modeling effort as well as radically simplifies the fabrication and mechanical complexity, rendering the approach suitable for small and lightweight robots.

*2) Joint Kinematics and Response:* The joint kinematics and its torque response are analyzed for their compatibility with the demands for the robot's bimodal operation.

As illustrated in Fig. 2A, link 1, with length  $l_1$  serving as a mechanical ground, is part of the airframe. Link 2, with length  $l_2$ , is attached to link 1 via a free revolute joint with the rotation angle  $\gamma$  ( $\gamma = 0^\circ$  when both links are parallel) and constrained by the joint limits to  $0^\circ \leq \gamma \leq 90^\circ$ . An elastic component with the original length of  $l_0$  connects the root of link 1 to the tip of link 2. Under this definition, the joint angle is  $90^\circ$  in the rolling mode and  $\gamma = 0^\circ$  in the flight mode.

To compute the restoring torque, the length of the elastic component  $l_e$  is found as a function of the linkage angle  $\gamma$  as:

$$l_e(\gamma) = \sqrt{(l_2 \sin \gamma)^2 + (l_1 + l_2 \cos \gamma)^2}. \quad (1)$$

Assuming the deformation of the elastic element follows the Hooke's law with stiffness  $k_e$ , the restoring force obeys  $F_e = k_e(l_e - l_0)$ . The force  $F_e$  provides a restoring torque on the revolute joint as

$$\tau_\gamma = F_e(l_1 l_2 / l_e) \sin \gamma = k_e(1 - (l_0 / l_e)) l_1 l_2 \sin \gamma. \quad (2)$$

In addition to the joint angle, it can be seen from Eq. (2) that the torque depends on several parameters, namely  $k_e$ ,  $l_1$ ,  $l_2$ , and  $l_0$ . The profile of  $\tau_\gamma$  versus  $\gamma$ , however, is independent

of  $k_e$ . To obtain better insights of the torque response, we rewrite Eq. (2) by introducing the parameterization  $l_0 = \alpha_0 l_2$  and  $l_1 = \alpha_1 l_2$ . This yields

$$\frac{\tau_\gamma}{k_e l_2^2} = \left( 1 - \frac{\alpha_0}{\sqrt{1 + \alpha_1^2 + 2\alpha_1 \cos \gamma}} \right) \alpha_1 \sin \gamma. \quad (3)$$

Eq. (3) provides a design guideline for evaluating suitable  $\alpha_0$  and  $\alpha_1$  that produce a desired torque profile. To simplify the process,  $\alpha_1$  is chosen as 0.2. The plot of normalized torque ( $\tau_\gamma / k_e l_2^2$ ) with respect to  $\gamma$  for different values of  $\alpha_0$  is shown in Fig. 2B. It can be observed that for a specific value of  $\alpha_0$ , there exists a particular  $0^\circ < \gamma^* < 90^\circ$  that maximizes the restoring torque. The condition corresponds to

$$\frac{d\tau_\gamma}{d\gamma}|_{\gamma^*} = 0 \quad \text{and} \quad \tau_\gamma^* = \tau_\gamma(\gamma^*). \quad (4)$$

The result implies that when the torque generated by propeller 2 or 4,  $\tau_\gamma = l_m T_{2,4}$  (see Fig. 2A,  $l_m$  is the length between the thrust vector and the revolute joint), is larger than  $\tau_\gamma^*$ , the propelling thrust overcomes the restoring torque and the revolute joint completely rotates to the flight configuration at  $\gamma = 0^\circ$ . The outcome is a consequence of the nonlinear torque response, which ensures that the robot reliably stays in the flying mode when

$$l_m T_{2,4} > \tau_\gamma^*, \quad (5)$$

Moreover, the relatively large value of  $\tau_\gamma / k_e l_2^2$  near the default state ( $\gamma = 90^\circ$ ) as seen in Fig. 2B guarantees that the propeller's axis remains perpendicular to  $Z_B$  when rotors 2 and 4 are minimally actuated or the robot operates in the terrestrial mode.

*3) Parameter Selection:* Notice that after selecting  $\alpha_1$ , while the critical joint angle  $\gamma^*$  illustrated in Fig. 2B varies with  $\alpha_0$ , it is independent of  $k_e$ . To select a suitable value of  $\alpha_0$ , we simultaneously consider the maximum anticipated strain (at  $\gamma = 0^\circ$ ) of the elastic component based on Eq. (1):  $\epsilon^* = (1 + \alpha_1 - \alpha_0) / \alpha_0$ , which is plotted in Fig. 2C for  $\alpha_1 = 0.2$ . It suggests that a smaller value of  $\alpha_0$  (which is preferred for a larger restoring torque when  $\gamma = 90^\circ$  as evidenced in Fig. 2B) would require an increasingly large deformation from the elastic element. This could potentially violate the proportional or elastic limit of the material. In this work,  $\alpha_0$  is chosen as 0.83 (highlighted in Fig. 2C) to balance the conflicting requirements.

Next, as determined by Eq. (5) and illustrated in Fig. 2B, it is critical to ensure that the propellers 2 and 4 produce sufficiently large thrust to *activate* the passive joints when flying. Hence, we consider the nominal condition for the hovering state such that  $T_{2,4} \approx mg/4$ , when  $mg$  is the weight of the vehicle. To ensure Eq. (5) is satisfied, we adopt a design parameter  $\alpha_m \in (0, 1)$  so that Eq. (5) becomes

$$\alpha_m \cdot mgl_m / 4 = \tau_\gamma^*. \quad (6)$$

Since  $\tau_\gamma^*$  is proportional to  $k_e$ , Eq. (6) is used to evaluate the linear stiffness  $k_e$  according to  $\alpha_m$  and the robot's mass. Under the Hooke's law assumption, the stiffness of the elastic element could be tuned via its geometry and properties:

$$k_e = EA_e / l_0 = EA_e / (\alpha_0 l_2), \quad (7)$$

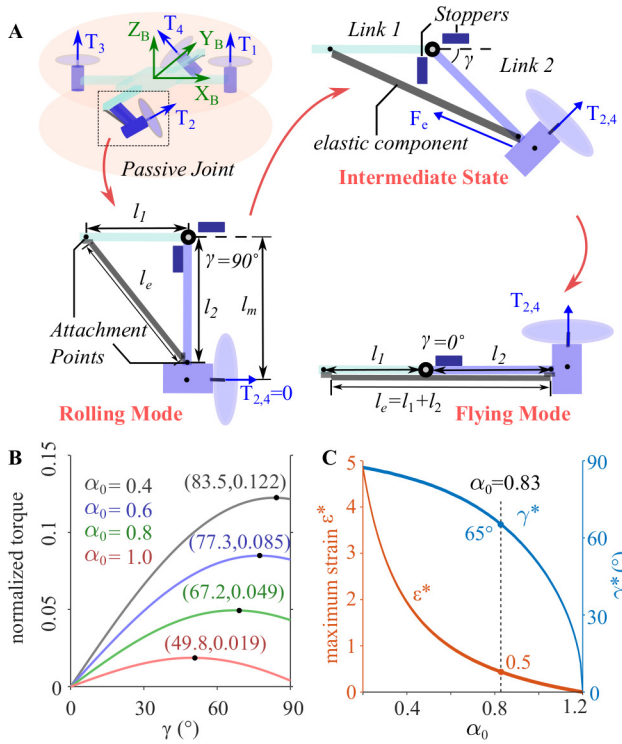


Fig. 2. (A) Diagrams illustrating the mechanism of the compliant folding joint. (B) Torque generated by the elastic component at different values of  $\alpha_0$ . (C) Maximum strain  $\epsilon^*$  and the joint angle  $\gamma^*$  at the maximum restoring torque  $\tau^*$  versus  $\alpha_0$ .

where  $E$  is the elastic modulus and  $A_e$  is the cross-sectional area. Since  $\alpha_0$  has been chosen, this leaves  $A_e$  as a free parameter to adjust for obtaining the desired  $k_e$  given  $\alpha_m$ .

### III. DYNAMIC MODELING AND CONTROL

In this section, we consider different states of the robot. The modeling of the robot in different configurations is discussed in the sequential order, starting from taking off, flying, transitioning to rolling, and then transitioning back to flight.

#### A. Taking off and Flying

From the default resting state with two passive joints inactivated (Fig. 1A), the robot passively reconfigure to the flight mode (Fig. 1B) once the motor commands are applied. During flight, the dynamics of the vehicle is similar to a conventional quadrotor, and thus, the controller from [40] is adopted. Other high-performance controllers and consideration of aerodynamic drag for high-velocity, more acrobatic maneuvers [4], [10] can be applied if required.

#### B. Transition from Flying to Rolling

The transformation from flight to rolling is realized by using the propellers' thrust to induce the vehicle to *flip* about a horizontal axis after landing as depicted in Fig. 3B to D.

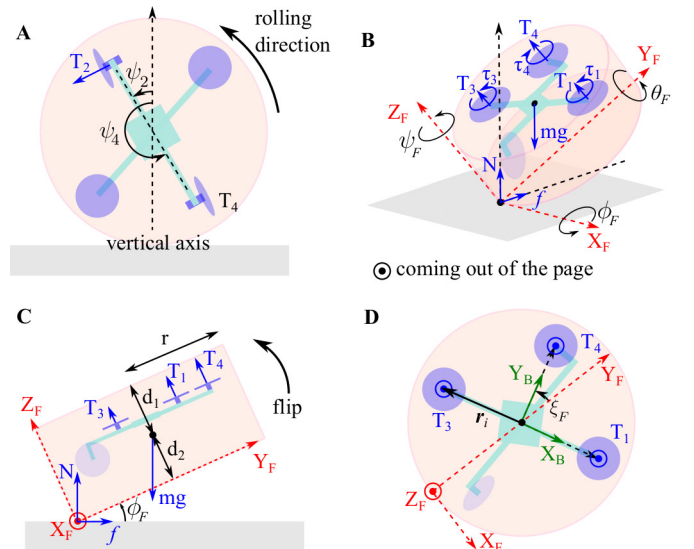


Fig. 3. (A) The vehicle in the mono-wheel state rolling on the ground. (B) The free body diagram of the robot during flipping. The non-inertial frame  $\mathcal{F}$  is defined for describing the fly-to-roll process, during of which the torque along the  $Z_F$  axis is balanced by the propeller induced torque. (C) The side view of the vehicle during flipping shows the torque about the  $X_F$  axis. (D) The top view of the robot as seen from the  $Z_F$  axis illustrates the torque balance along the  $Y_F$  axis.

**1) Flipping Dynamics:** The transitioning process is modeled based on the non-slip condition at the contact point between the robot and the ground. To simplify the analysis, we define another body-attached frame  $\mathcal{F} = \{X_F, Y_F, Z_F\}$  with the origin located at the ground contact and  $X_F$  coincident with the axis of the flipping motion as shown in Fig. 3B. We let  $\phi_F$  be the *flipping angle* as described in Fig. 3B and  $\xi_F$  indicate the flipping direction (angle from  $Y_F$  to  $Y_B$  measured about  $Z_B$  as seen in Fig. 3D). The goal is to command the robot to reorient  $\phi_F$  from  $0^\circ$  to  $90^\circ$  while suppressing the rotations about  $Y_F$  and  $Z_F$ .

To achieve the transition, the rotational dynamics of the frame  $X_F Y_F Z_F$  is obtained by linearizing about the point  $\theta_F, \psi_F = 0$  (see Fig. 3B). This can be approximately achieved as long as both  $\theta_F$  and  $\psi_F$  are actively minimized. Under such condition, the flipping dynamics are given by

$$\tau_F = \mathbf{J}_F [\ddot{\phi}_F \quad \ddot{\theta}_F \quad \ddot{\psi}_F]^T + mg(r \cos \phi_F - d_2 \sin \phi_F) \mathbf{e}_1, \quad (8)$$

where  $\mathbf{e}_j$ 's are basis vectors,  $\mathbf{J}_F$  is the tensor of inertia of the vehicle in the  $X_F Y_F Z_F$  frame,  $r$  is the radius of the wheel,  $d_2$  is the height of the center of mass as shown in Fig. 3C, and  $\tau_F$  is the collective torque generated by the propellers measured in the  $X_F Y_F Z_F$  frame. Subsequently, it is straightforward to derive a linear control law to stabilize the robot to the desired setpoint:  $\phi_F \rightarrow \phi_{F,d}$  and  $\theta_F, \psi_F \rightarrow 0$  as

$$\begin{aligned} \tau_F = & \mathbf{J}_F \ddot{\phi}_{F,d} \mathbf{e}_1 + mg(r \cos \phi_F - d_2 \sin \phi_F) \mathbf{e}_1 \\ & - \mathbf{K}_{F,d} \begin{bmatrix} \dot{\phi}_F - \dot{\phi}_{F,d} \\ \dot{\theta}_F \\ \dot{\psi}_F \end{bmatrix} - \mathbf{K}_{F,p} \begin{bmatrix} \phi_F - \phi_{F,d} \\ \theta_F \\ \psi_F \end{bmatrix}, \end{aligned} \quad (9)$$

in which  $\mathbf{K}_{F,d}$  and  $\mathbf{K}_{F,p}$  are positive diagonal gain matrices. The feedback of  $\phi_F$  and  $\dot{\phi}_F$  could be immediately determined from IMU data and the desired flipping direction angle  $\xi_F$ .

2) *Flipping Torque Generation*: Given the desired control torque from the controller, the next step is to determine the corresponding motor commands. This is different from the flight situation as  $\tau_F$  is defined with respect to frame  $\mathcal{F}$ .

The torque  $\tau_F$  is divided into four components  $\tau_F = \sum_{i=1}^4 \tau_{F,i}$  according to the contribution from the  $i^{\text{th}}$  propeller. Let  $\mathbf{r}_i$  be a vector representing the location of the  $i^{\text{th}}$  propeller in body frame and  $T_i$  be the magnitude of the thrust generated, then  $\tau_{F,i}$  is the sum of the torque attributed to the propelling thrust and the aerodynamic drag:

$$\begin{aligned}\tau_{F,i} &= (\mathbf{r}\mathbf{e}_1 + \mathbf{R}_z(\xi_F)\mathbf{r}_i) \times T_i\mathbf{e}_3 + c_\tau T_i\mathbf{e}_3 \\ &= ((\mathbf{r}\mathbf{e}_1 + \mathbf{R}_z(\xi_F)\mathbf{r}_i) \times \mathbf{e}_3 + c_\tau \mathbf{e}_3) T_i,\end{aligned}\quad (10)$$

where  $\mathbf{R}_z(\xi_F)$  is rotation matrix about the  $z$  axis, and  $c_\tau$  is a constant parameter mapping the propeller thrust to drag torque.

With four propellers contributing to  $\tau_F$ , the mapping between  $T_i$ 's and  $\tau_F$  is nominally under-determined. This allows us to introduce one constraint to render the torque generation deterministic. The constraint is chosen to reduce the possible slippage between the frame and the ground (in the direction perpendicular to  $X_F$ ). This is achieved by minimizing the horizontal force component. This translates to switching off the motor that is instantaneously closest to the ground contact point:

$$T_k = 0 \quad \text{for } k = (\lfloor 2\xi_F/\pi + 3/2 \rfloor \bmod 4) + 1, \quad (11)$$

with  $\lfloor \cdot \rfloor$  denoting the floor function. Note that in this thrust distribution, we have assumed that both passive joints are in the flight mode. In practice, this may be intermittently violated ( $T_{2,4} < \alpha_m mg/4$ ), depending on the actual torque command, the flipping angle  $\phi_F$ , and direction  $\xi_F$ . This can be further avoided by having a preferred flipping direction  $\xi_F = \pi$  or  $0$ , such that the  $T_1$  or  $T_4$ , which are associated with the revolute joints, would be relatively large and far from the off condition prescribed by Eq. (11) during the transition.

### C. Terrestrial Locomotion

The rolling motion is dictated by the torque about the  $Z_B$  axis generated by  $T_2$  and  $T_4$  and ground friction. This is realized via a simple open-loop policy. Either propeller 2 or 4 is activated at a time when its thrust force is aligned with the forward direction. That is,

$$T_i = \begin{cases} T_r \cos \psi_i & \psi_i \in (-\pi/2, \pi/2) \\ 0 & \text{otherwise} \end{cases}, \quad (12)$$

for  $i = \{2, 4\}$ , where  $\psi_i$  is the angle between the vertical and the current state of propeller  $i$  as shown in Fig. 3A. To ensure that propellers 2 and 4 remain in the rolling state, the amplitude  $T_r$  must be compatible with the design constraint given by Eq. (5):  $T_r < \tau_\gamma^*/l_m$ . In other words, the robot is only minimally actuated to realize the terrestrial locomotion.

With the reduced body width in the rolling mode, the robot is capable of passing through a narrow gap. However, in

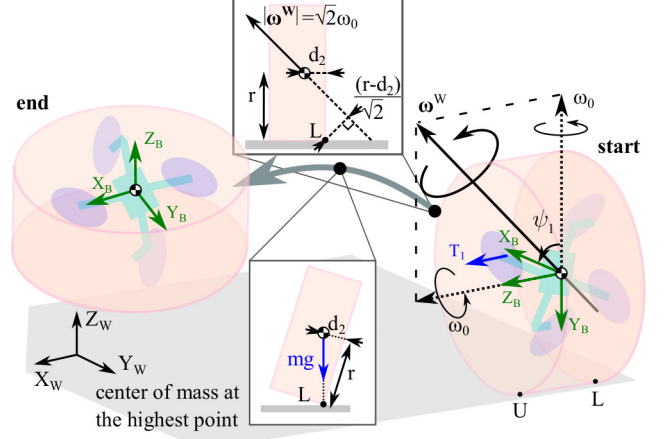


Fig. 4. A schematic drawing of the roll-to-fly transition in the world frame  $\mathcal{W}$ . The robot starts by rolling about its body axis  $Z_B$  at the speed  $\omega_0$ . An impulse torque about the vertical axis is applied via propeller 1 ( $T_1$ ), resulting in the total angular velocity (with respect to frame  $\mathcal{W}$ ) of  $\omega^W = [\omega_0, 0, \omega_0]^T$ , and the translational speed with non-slip condition is  $(r - d_2)\omega_0$ . Subsequently, the robot rotates into the flight-ready state with  $Z_B$  pointing upwards. Inset shows the state of the robot in the middle of the rotation when the center of mass is at the highest point.

the current design, the robot is unable to execute a precise controlled turn. To workaround, it is capable of repeatedly changing between two modes of locomotion as detailed below.

### D. Transition from Rolling to Flying

Unlike the conversion from aerial to terrestrial configurations, the roll-to-fly maneuver cannot be directly realized as the robot is unable to generate torque in the negative  $X_F$  direction (see Fig. 3) when it is in the rolling state. However, the robot is able to induce the rolling torque ( $Z_B$ ) and the positive torque about the vertical axis at some particular moment. As a consequence, we exploit the nonlinear property of a rotation to make the transition from rolling to flight using a devised maneuver concerning a simultaneously rotation about two body axes to workaround the limitation as described below.

1) *Rotation for rolling-to-flying transition*: To describe the intended maneuver, we inspect the rotational kinematics and associated dynamics. This begins by considering the robot with its current attitude state shown in Fig. 4. Therein, the robot is initially rolling with the angular speed  $\omega_z^B = \omega_0 > 0$  (about its  $Z_B$ ). In this state, the robot can be regarded as a vector of angular momentum that lies parallel to the  $X_W$  axis in the inertial frame  $\mathcal{W} = \{X_W, Y_W, Z_W\}$ . To begin the transition at the moment  $Y_B$  is downward, propeller 1 ( $T_1$ ) is momentarily actuated to create an impulse torque in the vertical ( $Z_W$ ) direction. The impulse induces a finite amount of vertical component to the angular momentum. Meanwhile, the resultant angular momentum can be expressed as a product of the inertia tensor and the angular velocity vector as seen in the inertial frame. Since the orientation of the robot remains the same immediately before and after the impulse is applied, this implies that the change in the angular momentum is due to the change in the angular velocity. In other words, a vertical

component is added to the angular velocity vector. Assuming the magnitude of the impulse torque is controlled (using the strategy described below), it is possible to ensure that the resultant angular velocity of the robot, measured with respect to the inertial frame, becomes  $\omega^W = [\omega_0, 0, \omega_0]^T$  as illustrated in Fig. 4. After this stage, the  $Z_B$  axis of the robot evolves from its initial state  $Z_B(t=0) = e_1$  with respect to  $\mathcal{W}$  thanks to  $\omega^W$  according to

$$\begin{aligned} Z_B(t) &= \cos(\omega_0 t) e_1 + \sin(\omega_0 t) e_2 \\ &\quad + (1/2)(1 - \cos(\omega_0 t))(e_1 + e_3), \end{aligned} \quad (13)$$

where we have assumed external torque to be negligible. As the rotation has reached  $180^\circ$  or  $\omega_0 t = \pi$ , we find  $Z_B = e_3$ . This indicates the robot is upright and ready for flight as depicted in Fig. 4.

In other words, starting from rolling at the angular speed,  $\omega_0$ , an impulse torque about the vertical axis to generate the resultant angular velocity  $\omega^W = [\omega_0, 0, \omega_0]^T$  would allow the robot to subsequently transition to the flight configuration if no external torque is applied. In non-ideal situations,  $Z_B$  can eventually reach the state  $Z_B(t) = e_3$  as long as  $\omega^W$  has a positive component in the third element.

*2) Minimum rotational speed for transition:* The rotation described above neglects the translational dynamics of the robot and other external forces such as friction and gravity. To obtain a bound of the minimum value of  $\omega_0$  that is required for a successful transition with external factors, we consider the conservation of energy.

Recall that immediately after receiving the impulse torque, the angular velocity of the robot is  $\omega^W = [\omega_0, 0, \omega_0]^T$  as seen in Fig. 4. During the transition, only the lower frame is in contact with the ground at point  $L$ . Assuming the non-slip condition at the contact point  $L$ , the instantaneous translational speed can be computed using the perpendicular distance between point  $L$  and the angular velocity vector  $\omega^W = [\omega_0, 0, \omega_0]^T$  as shown in Fig. 4 as  $(r - d_2)/\sqrt{2}$ . Since,  $|\omega^W| = \sqrt{2}\omega_0$ , the translational speed becomes  $(r - d_2)\omega_0$ . The total kinetic energy is given by  $\frac{1}{2}I_x\omega_0^2 + \frac{1}{2}I_z\omega_0^2 + \frac{1}{2}m\omega_0^2(r - d_2)^2$ , where  $I_x, I_y, I_z$  are the principal moments of inertia. As illustrated in Fig. 4, in the middle of the transition, only the lower frame is in contact with the ground at point  $L$ . The center of mass of the robot is displaced from the height of  $r$  (from the rolling state) to the highest point of  $\sqrt{r^2 + d_2^2}$ . Therefore, if one assumes all kinetic energy is converted into the potential energy, the minimum value  $\omega_0$ , denoted  $\omega_0^*$ , required for the transition can be computed from

$$\frac{1}{2}(I_x + I_z + m(r - d_2)^2)\omega_0^{*2} = mg\left(\sqrt{r^2 + d_2^2} - r\right). \quad (14)$$

For the prototype presented below in Section IV with the inertia listed in Table S1, Eq. (14) predicts the minimally required  $\omega_0^*$  to be 3.9 rad/s. In practice, we anticipate the value of  $\omega_0^*$  to be higher as not all kinetic energy would be converted to potential energy during the transition and there exist viscous losses (friction included) in the process. Nevertheless, the computed  $\omega_0^*$  still serves as a crude guideline.

*3) Impulse torque generation:* The dynamic maneuver for the robot to make a roll-to-fly transition described above starts with the robot rolling at the rate of  $\omega_0$ . To suddenly create the desired angular velocity  $\omega^W = [\omega_0, 0, \omega_0]^T$ , it has been assumed that an impulse torque about the vertical axis is generated by a sudden actuation of propeller 1. In practice, this can only be approximately achieved.

To generate the vertical torque resembling an impulse in an actual experiment, we propose the following feedback driving scheme command:

$$T_1 = \begin{cases} (1 + \omega_y^B/\omega_0) T^+ \sin^3 \psi_1 & \text{for } \psi_1, \omega_0 + \omega_y^B > 0 \\ 0 & \text{otherwise} \end{cases} \quad (15)$$

where  $\psi_1$  is the angle between  $X_B$  (arm of propeller 1) and  $Z_W$  axes measured about  $Z_B$  (see Fig. 4) and  $T^+$  is the maximum thrust the propeller can generate. The piecewise form of Eq. (15) serves three purposes. First, the dependence on  $\psi_1$  ensures that the torque generated is always positive about  $Z_B$  as intended. Second, the sine function renders the thrust (and, hence, the impulse torque) maximum when  $\psi_1 = \pi/2$ . The cubic form creates a sharp but smooth and continuous peak, resembling an impulse. Lastly, the term  $1 + \omega_y^B/\omega_0$  can be regarded as a one-way proportional control term to drive  $\omega_y^B$  towards  $-\omega_0$ .

All in all, the proposed transitioning maneuver begins with the robot in a rolling state with the angular speed  $\omega_0$ . The transition is induced by the realization of the intended angular velocity  $\omega^W = [\omega_0, 0, \omega_0]^T$ , which is obtained using an impulse-like feedback motor command detailed by Eq. (15). Meanwhile, the threshold for the minimally required speed or  $\omega_0^*$  is calculated from the conservation of energy, neglecting frictional and other losses. Remark that, thanks to the symmetry of the robot, an identical maneuver can also be accomplished when the axis  $Y_B$  in Fig. 4 is directed upwards. In that circumstance, a similar motor command must be provided to propeller 3, instead of propeller 1.

#### IV. PROTOTYPE MANUFACTURING AND CHARACTERIZATION OF PASSIVE JOINTS

The fabrication of the hybrid quadrotor is detailed, followed by the discussion of the design and mechanical properties of the passive joints.

##### A. Airframe and Robot Construction

The wheel-like protective frame was manufactured from a 2-mm-thick carbon fiber sheet and carbon fiber rods (2 mm diameter). The radius of the rolling frame is  $r = 90$  mm and the robot's height is  $d_1 + d_2 = 75$  mm, with  $d_2 = 30$  mm. The robot is capable of rolling through a gap narrower than its 180-mm diameter.

For actuation and avionics, we employed four 1104 brushless 7500-KV motors and 2-inch 4-blade propellers. The motors were symmetrically mounted with the distance from the central axis of  $r_m = 54$  mm. A programmable flight control board (Bitcraze, Crazyflie Bolt) together with a 4-in-1 electronic speed controller (DALRC, Engine Pro 40A)

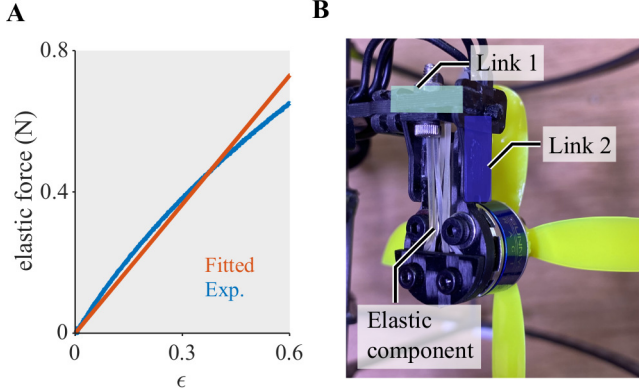


Fig. 5. (A) Force profile of a single rubber band. The fitted stiffness in the region of  $\epsilon \in [0, 0.5]$  is 98 N/m. (B) The revolute joint with two rubber bands attached.

were used for locomotion control and powered by a 1300 mAh 2S battery. The total mass of the quadrotor in Fig. 1 is about 156 g. All physical parameters of the robot are listed in Table. S3. The moments of inertia were experimentally estimated as described in the Supplementary Materials.

#### B. Revolute Joint Fabrication and Characterization

The joint design begins with selecting the length  $l_2 = 15$  mm as the baseline. Shorter length complicates the manufacturing, whereas a larger number would excessively increase the robot's size. With  $\alpha_0 = 0.83$  chosen in Section II (Fig. 2), the relaxed length of the elastic component is  $l_0 = 12$  mm.

The dimension of the elastic element determines the linear stiffness  $k_e$  as captured by Eq. (7). Meanwhile,  $k_e$  must satisfy the switching criteria set out by Eq. (6). Opting for  $l_m = l_2$  and selecting  $\alpha_m \approx 0.4$ , we obtain the target  $k_e$  about 170 N/m. Small elastic rubber bands with the diameter of 7.9 mm were adopted to act as the elastic elements. When the rubber band was affixed to link 1 and link 2, the theoretical relaxed length is  $l_0 = 7.9\pi/2 = 12.4$  mm. This is sufficiently close to the intended  $l_0$  of 12 mm.

The effective stiffness of the elastic elements was measured with a universal testing machine (5942, Instron) at low speed to minimize the viscoelastic effect. We identified the linear stiffness of 98 N/m (fitted line in Fig. 5A) for one rubber band. To yield the desired stiffness, two bands were mounted to the passive switching joint as shown in Fig. 5B. The effective stiffness of the total elastic component is  $k_e = 196$  N/m, and the  $\alpha_m$  is 0.46. The point of mechanical failure is near the strain value  $\epsilon$  of 7.5, considerably above the intended operating range of  $\epsilon^* = 0.5$  shown in Fig. 2B. This ensures that the rubber bands are in its elastic region in operations.

Next, the fabricated passive joints were tested for the passive rotation. We found that the critical propelling thrust for the joint rotation ( $T_{2,4} = \tau_\gamma^*/l_m$ ) was 0.29 N. Compared to the expected thrust during hovering,  $T_i = mg/4 = 0.39$  N, the thrust ratio  $\alpha_m$  from Eq. (6) is 0.74. This is higher than the intended value of 0.46 likely due to the weight of the link and motor neglected in the model. Nevertheless, it is

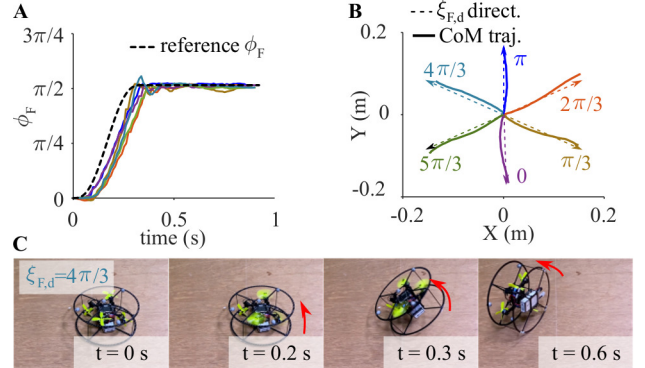


Fig. 6. Fly-to-roll demonstration. (A) Flipping angle  $\phi_F$  of the robot over time. Multiple lines refer to different flapping directions  $\xi_{F,d}$ . (B) The trajectory of the center of mass for different  $\xi_F$  setpoints. (C) Sequential images illustrating the maneuver for the case  $\xi_F = 4\pi/3$ .

considerably below unity and should not adversely affect the flight performance.

#### V. EXPERIMENTAL VALIDATION

In this section, we realized the transition from flying to rolling based on the devised strategy. Then, the roll-to-fly transition was experimentally demonstrated and the outcomes are compared with the simulated results from the developed dynamic model. Finally, the bimodal operation of the robot was conducted to highlight the ability of the robot to pass through a narrow gap by rolling.

##### A. Experimental Setup

To perform indoor experiments, retroreflective markers were employed to leverage the position feedback from the motion capture cameras (Prime 13w, Optitrack) when needed. The ground station transmitted the position data to the robot via radio communication.

##### B. Fly-to-Roll Transition

The transition from flying to rolling was conducted with the robot initially resting on the ground with  $Z_B$  pointing up. The flipping was achieved using the PD control law described by Eqs. (9)-(11) using primarily the IMU feedback. To assure a smooth maneuver, a reference trajectory of the flipping angle  $\phi_F(t)$  was generated with a fourth-order polynomial function and uploaded to the robot onboard controller. Only the flipping direction feedback  $\xi_F$  (equivalent to the yaw angle) was provided by the motion capture system. Since the proposed thrust mapping has a preference on the angle  $\xi_F$  (near 0 or  $\pi$  is favorable), we conducted the test at six flipping directions  $\xi_F = 0, \pi/3, 2\pi/3, \pi, 4\pi/3$ , and  $5\pi/3$ .

As shown in Fig. 6 and Video S1, the robot took less than one second to successfully transition from all directions ( $\phi_F$  increased from 0 to  $\pi/2$ , Fig. 6A). During the process, the trajectories of the center of mass displaced along the intended directions  $\xi_F$  as visualized in Fig. 6B. The results validate the performance of the proposed linear control law and the propelling thrust mapping detailed in Section III-B, irrespective of the flipping direction  $\xi_F$ .

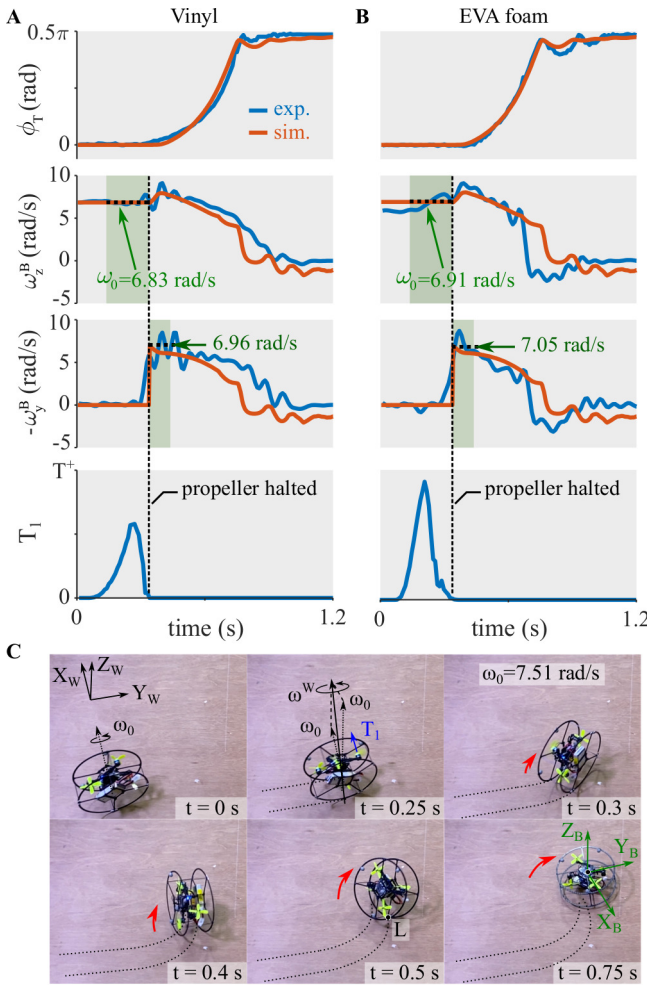


Fig. 7. Plots of  $\phi_T$ ,  $\omega_z^B$  and  $-\omega_y^B$  of the roll-to-fly transitioning maneuver performed on (A) vinyl flooring and (B) EVA foam. The plots show the data taken from the experiments (blue) and dynamic simulation (red). The experimental data were shown after being low-pass filtered for clarity. Green regions are used for calculating (averaging)  $\omega_0$  and its uncertainty. (C) An image sequence demonstrating the roll-to-fly maneuver on plywood with  $\omega_0 = 7.51$  rad/s, with red arrows indicating the direction of the transition.

### C. Roll-to-Fly Maneuver

The transition from rolling to flying configuration is dynamically accomplished to work around the limitation on the inability of the robot to generate the body torque in the negative  $X_F$  direction (Fig. 3) when it is rolling as elaborated in Section III-D. The devised solution can be approximately realized using the torque generation scheme detailed by Eq. (15). To validate the effectiveness of the devised scheme, both experiments and dynamic simulation were carried out.

To execute the roll-to-fly maneuver, the robot was controlled to roll at 16 different  $\omega_0$  speeds ranging from 0 to  $4\pi$  rad/s over three kind of ground surfaces: vinyl flooring, plywood, and EVA foam. The static friction coefficients of these materials are approximately 0.2, 0.4, and 0.8, respectively (see Supplementary Materials). In each trial, the robot was commanded to roll at a particular  $\omega_z^B = \omega_0$  speed. The motor command for generating the vertical torque described by Eq. (15) was used, with the angular rate feedback from the IMU, to swiftly drive  $\omega_y^B$  (Fig. 4) to  $-\omega_0$  as intended. Once the

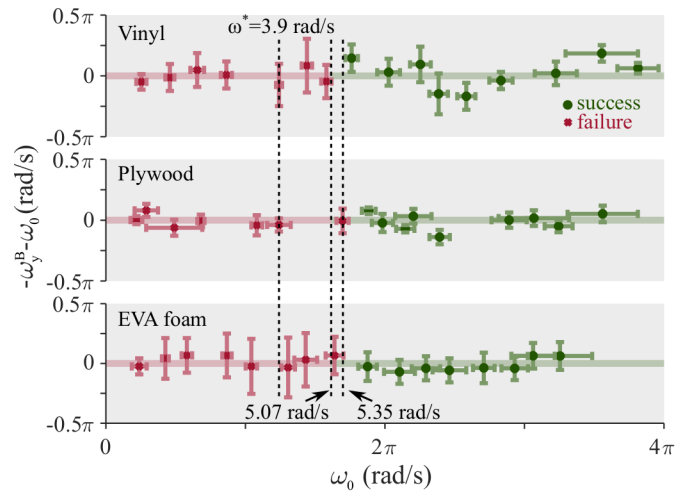


Fig. 8. Simulation (thick lines) and experimental (markers) results of the roll-to-fly tests. Green and red colors represent successful and failed transitions. The x axis indicates the rolling speed ( $\omega_z^B = \omega_0$ ) of the robot and the y axes describes the difference between  $-\omega_y^B$  and the desired turning rate  $\omega_0$ . The experimental success rate is 100% when  $\omega_0 > 5.35$  rad/s. The threshold is slightly lower (5.07 rad/s) for the simulation. The bound calculated from the conservation of energy is  $\omega_0^* = 3.9$  rad/s.

magnitude of  $\omega_y^B$  was perceived to be equal to the current rolling rate  $\omega_0$ , the motor command was stopped and the transition began. For  $\omega_0$  beyond  $4\pi$ , it becomes increasingly challenging for the robot to generate the impulse for  $\Omega$  to match  $\omega_0$  in a short time.

For the simulation, an open-source physics engine PyBullet [41] commonly used for robotics research, was adopted. The robot was created as a cylindrical object with its mass and inertia properties, as well as the location of the center of mass, matched to the actual robot. The coefficient for contact friction between the robot and the ground was set to 0.2 (the results were found to be insensitive to this coefficient within the range 0.1 to 1.0) and other non-conservative forces were disabled. The transition was simulated by setting the initial rolling speed of the robot to  $\omega_0$ , making the robot roll in a straight line. Next, the turning speed ( $\omega_y^B$ ) was suddenly changed from 0 to precisely  $-\omega_0$ , imitating the desired consequence of the vertical impulse torque. We tracked the motion of the body axis  $Z_B$  to determine whether the transition is successful.

To quantify the behavior of the robot during the transition, we define  $\phi_T$  as the angle between  $Z_B$  and the horizontal plane:  $\phi_T = \pi/2 - \arccos(Z_B \cdot Z_W)$ . Figure 7A shows the trajectory of the robot during the experiment on vinyl flooring as the ground alongside the simulation result when the rolling velocity  $\omega_0$  was 6.83 rad/s. Similarly, the case of EVA foam surface with  $\omega_0 = 6.91$  rad/s is illustrated in Figure 7B. It can be seen that in both examples, the approximate impulse command increased the turning rate  $-\omega_y^B$  of the robot to the desired level ( $\omega_0$ ) in approximately 0.1 s. Once  $\omega_z^B$  and  $-\omega_y^B$  are approximately equal, the dynamic maneuver started and  $\phi_T$  increased from zero towards  $90^\circ$ . In both occurrences, the robot finished the transition in  $\approx 0.5$  s. The trajectories of the robot from the experiments are highly similar to the simulation results. However, for the simulation, it takes longer than 1.2

s for the angular speeds to settle to zero at the end due to the absence of other viscous forces. Fig. 7C shows the robot performing the transitioning maneuver on plywood with  $\omega_0 = 7.51$  rad/s. More examples can be found in Video S1.

From the total of 48 trials over three ground surfaces (16 each), the summary of the experimental results is presented in Fig. 8. The plots show whether the transition was successfully achieved at each rolling speed  $\omega_0$ . For each data point, the value  $\omega_0$  is taken as the mean ( $\pm$  standard deviation) derived from the 0.2-s interval before the command to propeller 1 was halted (a vertical line in Fig. 7A and B). Furthermore, the vertical axes in Fig. 8 indicate the difference between the realized turning rate  $-\omega_y^B$  and its setpoint  $\omega_0$ :  $-\omega_y^B - \omega_0$ . The mean ( $\pm$  standard deviation) is computed the 0.1-s interval after the command to propeller 1 was halted. It can be seen that the uncertainty in  $\omega_0$  is relatively high at large  $\omega_0$  because the viscous losses made it difficult for the robot to retain its high rolling speed. On the other hand, the relatively large standard deviations in  $-\omega_y^B - \omega_0$  on the EVA foam at low rolling speeds were due to the difficulty to reach the desired  $-\omega_y^B$  setpoints in the presence of large friction. On the same plots, the outcomes from the simulation (shown as lines) are also shown. For the simulation  $-\omega_y^B - \omega_0$  is always zero as an ideal impulse torque was assumed.

The findings from the experiments and the simulation are largely consistent. As shown in Fig. 8, out of 26 experimental trials over three types of surfaces with  $\omega_0 > 5.35$  rad/s, all of them were successful. The value of  $\omega_0 > 5.35$  rad/s is somewhat higher than the threshold of  $\omega^* = 3.9$  rad/s computed by the conservation of energy or Eq. (14). This is anticipated as total kinetic-to-potential energy conversion was assumed and frictional loses were neglected. For the simulation, which makes use of high-fidelity dynamic models, the transition is predicted to be successful as long as  $\omega_0 > 5.07$  rad/s. The small discrepancies between the simulation and experimental results are likely due to other non-conservative forces and uncertain model parameters (such as the moment of inertia). However, both simulation and experimental results suggest that the transition is not critically influenced by the friction coefficient as long as the desired angular velocity can be realized based on the outlined driving command for the propeller.

#### D. Hybrid Aerial-Terrestrial Trajectory

To validate that the flight performance of the robot is unaffected by the passive joints and manifest the unique capability of the robot, we designed a bimodal trajectory. The path contains a short middle section that the robot with the diameter of 18 cm must traverse through a 10-cm gap. As such, the vehicle was instructed to roll through the passage before continuing its flight afterwards. The 10-cm aperture is too narrow for other multirotor MAVs to fly or roll through.

As captured by Fig. 9 and the hybrid trajectory experiment part of Video S1, the robot started the trajectory tracking by taking off from the ground to the height of 0.6 m. During this, the motor commands were gradually ramped up ( $\approx 1$  s) to allow two passive joints to smoothly re-orient for flight. The robot

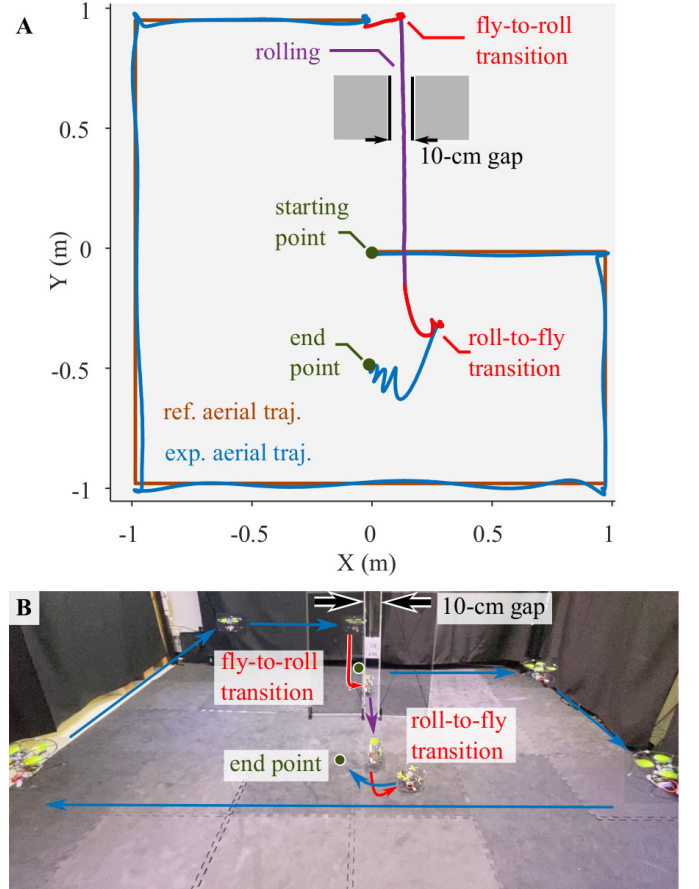


Fig. 9. (A) Reference and realized trajectory from the hybrid locomotion experiment with the gap size of 10 cm. (B) A composite image showing the robot during different stages of the trajectory.

then flew for approximately 7 m along the perimeter of the arena before landing behind the gap created by two simulated walls (constructed with carbon fiber rods and transparent for visibility). With the knowledge of the gap's location, the landing position and yaw angle can be strategically chosen as detailed in Fig. S4 (Supplementary Materials). In this case, the flipping direction for the subsequent fly-to-roll transition was  $\xi_F \approx 0.13\pi$  (sufficiently far from the less desirable values of 0 or  $\pi$ ). The root mean square position error of the 30-second flight is 3.9 cm, suggesting that the flight performance is not detrimentally affected by the passive joints.

Thereafter, the robot executed the transition and safely negotiated through the 10-cm gap via rolling. Once emerged on the other side, it performed the roll-to-fly maneuver using the scheme detailed in Section III-D. The arena ground surface was EVA foam with  $\mu_s \approx 0.8$ . The robot completed the move in 2 s after using the rolling speed  $\omega_0$  of 5.8 rad/s. The experiment concluded with a final take-off, showing the robot resuming flight after rolling through the tight space.

The hybrid bi-modal experiment shows that the novel passive mechanism enables the quadrotor to seamlessly fly or roll according to the environments. In a simple test described in the Supplementary Materials, the robot reached the speed of up to 2.8 m/s ( $> 15$  body lengths/s) in the rolling motion. With the added functionality, the robot possesses exceptional

potential to operate in cluttered or challenging environments.

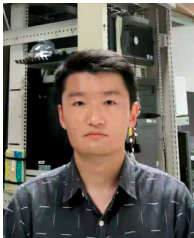
## VI. CONCLUSION

Driven by the need for aerial robots capable of operations in unstructured environments, we proposed a multirotor vehicle that leverages the protective frame for terrestrial locomotion. In the meantime, the robot relies on the passively reconfigurable airframe for altering the direction of the propelling thrusts to roll on the ground. The strategy enables the robot to travel through a passage too narrow to safely fly through. The passive mechanisms dispense the need for extra actuators but it brings about a challenge in the transition between two modes of locomotion. To resolve this, a dynamic maneuver has been modeled and developed for the robot to realize the flipping motion despite the inability to directly generate the torque in the required direction. A series of experiments were conducted to validate the bi-modal locomotion, including the transitions between the aerial and terrestrial modes. For future work, the terrestrial locomotion and the modal transitions can be improved for the robot to robustly operate in rugged or uneven terrains.

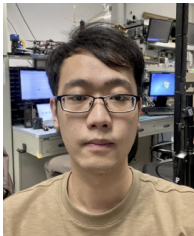
## REFERENCES

- [1] B. Zhou, J. Pan, F. Gao, and S. Shen, “Raptor: Robust and perception-aware trajectory replanning for quadrotor fast flight,” *IEEE Transactions on Robotics*, 2021.
- [2] S. Zhong and P. Chirarattananon, “An efficient iterated ekf-based direct visual-inertial odometry for mavs using a single plane primitive,” *IEEE Robotics and Automation Letters*, 2020.
- [3] P. Zheng, X. Tan, B. B. Kocer, E. Yang, and M. Kovac, “Tiltdrone: A fully-actuated tilting quadrotor platform,” *IEEE Robotics and Automation Letters*, vol. 5, no. 4, pp. 6845–6852, 2020.
- [4] S. H. Arul and D. Manocha, “Dcad: Decentralized collision avoidance with dynamics constraints for agile quadrotor swarms,” *IEEE Robotics and Automation Letters*, vol. 5, no. 2, pp. 1191–1198, 2020.
- [5] H. Xie, X. Cai, and P. Chirarattananon, “Towards cooperative transport of a suspended payload via two aerial robots with inertial sensing,” in *2020 IEEE/RSJ International Conference on Intelligent Robots and Systems (IROS)*, 2020, pp. 1215–1221.
- [6] B. Xian and S. Yang, “Robust tracking control of a quadrotor unmanned aerial vehicle-suspended payload system,” *IEEE/ASME Transactions on Mechatronics*, 2020.
- [7] H. Hua, Y. Fang, X. Zhang, and C. Qian, “A new nonlinear control strategy embedded with reinforcement learning for a multirotor transporting a suspended payload,” *IEEE/ASME Transactions on Mechatronics*, 2021.
- [8] Y. Tian, K. Liu, K. Ok, L. Tran, D. Allen, N. Roy, and J. P. How, “Search and rescue under the forest canopy using multiple uavs,” *The International Journal of Robotics Research*, vol. 39, no. 10-11, pp. 1201–1221, 2020.
- [9] C. Ding and L. Lu, “A tilting-rotor unmanned aerial vehicle for enhanced aerial locomotion and manipulation capabilities: Design, control, and applications,” *IEEE/ASME Transactions on Mechatronics*, 2020.
- [10] H. Jeon, J. Song, H. Lee, and Y. Eun, “Modeling quadrotor dynamics in a wind field,” *IEEE/ASME Transactions on Mechatronics*, 2020.
- [11] T. Tomić, C. Ott, and S. Haddadin, “External wrench estimation, collision detection, and reflex reaction for flying robots,” *IEEE Transactions on Robotics*, vol. 33, no. 6, pp. 1467–1482, 2017.
- [12] G. de Croon, C. De Wagter, and T. Seidl, “Enhancing optical-flow-based control by learning visual appearance cues for flying robots,” *Nature Machine Intelligence*, vol. 3, no. 1, pp. 33–41, 2021.
- [13] R. Ding, Y.-H. Hsiao, H. Jia, S. Bai, and P. Chirarattananon, “Passive wall tracking for a rotorcraft with tilted and ducted propellers using proximity effects,” *IEEE Robotics and Automation Letters*, vol. 7, no. 2, pp. 1581–1588, 2022.
- [14] H. V. Phan and H. C. Park, “Mechanisms of collision recovery in flying beetles and flapping-wing robots,” *Science*, vol. 370, no. 6521, pp. 1214–1219, 2020.
- [15] Z. Wang, Z. Qian, Z. Song, H. Liu, W. Zhang, and Z. Bi, “Instrumentation and self-repairing control for resilient multi-rotor aircrafts,” *Industrial Robot: An International Journal*, 2018.
- [16] Y. Chen, S. Xu, Z. Ren, and P. Chirarattananon, “Collision resilient insect-scale soft-actuated aerial robots with high agility,” *IEEE Transactions on Robotics*, 2021.
- [17] A. Briod, P. Kornatowski, J.-C. Zufferey, and D. Floreano, “A collision-resilient flying robot,” *Journal of Field Robotics*, vol. 31, no. 4, pp. 496–509, 2014.
- [18] Y. Mulgaonkar, A. Makineni, L. Guerrero-Bonilla, and V. Kumar, “Robust aerial robot swarms without collision avoidance,” *IEEE Robotics and Automation Letters*, vol. 3, no. 1, pp. 596–603, 2017.
- [19] P. Sareh, P. Chermpayong, M. Emmanuelli, H. Nadeem, and M. Kovac, “Rotorigami: A rotary origami protective system for robotic rotorcraft,” *Science Robotics*, vol. 3, no. 22, 2018.
- [20] J. Zha, X. Wu, J. Kroeger, N. Perez, and M. W. Mueller, “A collision-resilient aerial vehicle with icosahedron tensegrity structure,” in *2020 IEEE/RSJ International Conference on Intelligent Robots and Systems (IROS)*, 2020, pp. 1407–1412.
- [21] S. Mintchev, J. Shintake, and D. Floreano, “Bioinspired dual-stiffness origami,” *Science Robotics*, vol. 3, no. 20, 2018.
- [22] J. Shu and P. Chirarattananon, “A quadrotor with an origami-inspired protective mechanism,” *IEEE Robotics and Automation Letters*, vol. 4, no. 4, pp. 3820–3827, 2019.
- [23] Cao, Lin and Dolovich, Allan T and Schwab, Arend L and Herder, Just L and Zhang, Wenjun, “Toward a unified design approach for both compliant mechanisms and rigid-body mechanisms: Module optimization,” *Journal of Mechanical Design*, vol. 137, no. v12, p. 122301, 2015.
- [24] Wang, Fei and Qian, Zhiqin and Yan, Zhiguang and Yuan, Chenwang and Zhang, Wenjun, “A novel resilient robot: Kinematic analysis and experimentation,” *IEEE Access*, vol. 8, pp. 2885–2892, 2019.
- [25] V. Riviere, A. Manevy, and S. Viollet, “Agile robotic fliers: A morphing-based approach,” *Soft robotics*, vol. 5, no. 5, pp. 541–553, 2018.
- [26] D. Falanga, K. Kleber, S. Mintchev, D. Floreano, and D. Scaramuzza, “The foldable drone: A morphing quadrotor that can squeeze and fly,” *IEEE Robotics and Automation Letters*, vol. 4, no. 2, pp. 209–216, 2019.
- [27] T. Yang, Y. Zhang, P. Li, Y. Shen, Y. Liu, and H. Chen, “Sniaesse deformation mechanism enabled scalable multicopter: Design, modeling and flight performance validation,” in *2020 IEEE International Conference on Robotics and Automation (ICRA)*. IEEE, 2020, pp. 864–870.
- [28] N. Bucki and M. W. Mueller, “Design and control of a passively morphing quadcopter,” in *2019 International Conference on Robotics and Automation (ICRA)*. IEEE, 2019, pp. 9116–9122.
- [29] A. Kalantari and M. Spenko, “Modeling and performance assessment of the hytaq, a hybrid terrestrial/aerial quadrotor,” *IEEE Transactions on Robotics*, vol. 30, no. 5, pp. 1278–1285, 2014.
- [30] P. SA, *Parrot Minidrones Rolling Spider User Guide*, Parrot FA.
- [31] Zhang, Ruibin and Wu, Yuze and Zhang, Lixian and Xu, Chao and Gao, Fei, “TIE: An Autonomous and Adaptive Terrestrial-Aerial Quadrotor,” *arXiv preprint arXiv:2109.04706*, 2021.
- [32] Fabris, Amedeo and Kirchgeorg, Steffen and Mintchev, Stefano, “A Soft Drone with Multi-modal Mobility for the Exploration of Confined Spaces,” in *2021 IEEE International Symposium on Safety, Security, and Rescue Robotics (SSRR)*. IEEE, 2021, pp. 48–54.
- [33] Daler, Ludovic and Mintchev, Stefano and Stefanini, Cesare and Floreano, Dario, “A bioinspired multi-modal flying and walking robot,” *Bioinspiration & biomimetics*, vol. 10, no. 1, p. 016005, 2015.
- [34] Pratt, Christopher J and Leang, Kam K, “Dynamic underactuated flying-walking (DUCK) robot,” in *2016 IEEE International Conference on Robotics and Automation (ICRA)*. IEEE, 2016, pp. 3267–3274.
- [35] Ratsamee, Photchara and Kriengkomol, Pakpoom and Arai, Tatsuo and Kamiyama, Kazuto and Mae, Yasushi and Kiyokawa, Kiyoshi and Mashita, Tomohiro and Uranishi, Yuki and Takemura, Haruo, “A hybrid flying and walking robot for steel bridge inspection,” in *2016 IEEE International Symposium on Safety, Security, and Rescue Robotics (SSRR)*. IEEE, 2016, pp. 62–67.
- [36] Kuswadi, Son and Tamara, Mohamad Nasyir and Sahanas, Dzikri Aditya and Islami, Galang Ilham and Nugroho, Setyo, “Adaptive morphology-based design of multi-locomotion flying and crawling robot ‘PENS-FlyCrawl’,” in *2016 International Conference on Knowledge Creation and Intelligent Computing (KCIC)*. IEEE, 2016, pp. 80–87.
- [37] Anzai, Tomoki and Kojo, Yuta and Makabe, Tasuku and Okada, Kei and Inaba, Masayuki, “Design and Development of a Flying Humanoid Robot Platform with Bi-copter Flight Unit,” in *2020 IEEE-RAS 20th*

- International Conference on Humanoid Robots (Humanoids).* IEEE, 2021, pp. 69–75.
- [38] Orozco-Magdaleno, Ernesto C and Gómez-Bravo, Fernando and Castillo-Castañeda, Eduardo and Carbone, Giuseppe, “Evaluation of locomotion performances for a mecanum-wheeled hybrid hexapod robot,” *IEEE/ASME Transactions on Mechatronics*, vol. 26, no. 3, pp. 1657–1667, 2021.
- [39] K. Kawasaki, M. Zhao, K. Okada, and M. Inaba, “Muwa: Multi-field universal wheel for air-land vehicle with quad variable-pitch propellers,” in *2013 IEEE/RSJ International Conference on Intelligent Robots and Systems*. IEEE, 2013, pp. 1880–1885.
- [40] D. Mellinger and V. Kumar, “Minimum snap trajectory generation and control for quadrotors,” in *2011 IEEE international conference on robotics and automation*. IEEE, 2011, pp. 2520–2525.
- [41] Coumans, Erwin and Bai, Yunfei, “Pybullet, a python module for physics simulation for games, robotics and machine learning,” 2016.



**Huaiyuan Jia** received the B.S. degree in mechanical engineering from Shanghai Jiaotong University, Shanghai, China, in 2017. He was a research assistant with the Department of Automation, University of Science and Technology of China in 2019. He is currently pursuing the Ph.D. degree with the Department of Biomedical Engineering, City University of Hong Kong.



**Songnan Bai** received the B.S. degree in mechanical engineering from Xi'an Jiaotong University, Xi'an, China, in 2017 and the M.S. degree in mechanical engineering from City University of Hong Kong, Hong Kong. He is currently pursuing the Ph.D. degree with the Department of Biomedical Engineering, City University of Hong Kong.



**Runze Ding** received his B.S. degree in aircraft power engineering in 2015 and his M.Phil. degree in aerospace propulsion theory in 2019, both from Nanjing University of Aeronautics and Astronautics, Nanjing, China. He is currently pursuing the Ph.D. degree with the Department of Biomedical Engineering, City University of Hong Kong.



**Jing Shu** received the B.Eng. degree in mechatronic engineering from City University of Hong Kong, Hong Kong in 2019. He is currently pursuing the Ph.D. degree with the Department of Biomedical Engineering, The Chinese University of Hong Kong.



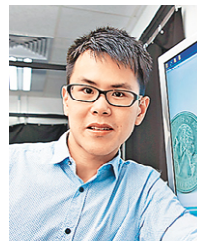
**Yanlin Deng** received her B.S. degree in Pharmaceutical Engineering in Southwest University, China, and M.S. degree in City University of Hong Kong, Hong Kong. She is currently pursuing the Ph.D. degree with the Department of Biomedical Engineering, City University of Hong Kong. Her research interests are focused on cancer research and microfluidics.



devices for personalized

**Bee Luan Khoo** received the B.S. degree in biomedical science from Nanyang Technological University, Singapore, and the Ph.D. degree in biomedical/medical engineering from National University of Singapore, Singapore. She was a postdoctoral associate in the Singapore-MIT Alliance for Research and Technology.

She is currently an Assistant Professor with the Department of Biomedical Engineering, City University of Hong Kong, Hong Kong. Her work includes the design and utilization of microfluidic cancer management and evaluation.



systems.

**Pakpong Chirarattananon** (S'12-M'15) received the B.A. degree in Natural Sciences from the University of Cambridge, U.K., in 2009, and the Ph.D. degree in Engineering Sciences from Harvard University, Cambridge, MA, USA, in 2014.

He is currently an Associate Professor with the Department of Biomedical Engineering, City University of Hong Kong, Kowloon, Hong Kong SAR, China. His research interests include bio-inspired robots, micro air vehicles, and the applications of control and dynamics in robotic

SUPPLEMENTAL MATERIALS FOR  
A QUADROTOR WITH A PASSIVELY RECONFIGURABLE AIRFRAME  
FOR HYBRID TERRESTRIAL LOCOMOTION

Huaiyuan Jia, Songnan Bai, Runze Ding, Jing Shu,  
Yanlin Deng, Bee Luan Khoo, and Pakpong Chirarattananon

Department of Biomedical Engineering,  
City University of Hong Kong,  
Tat Chee Avenue, Hong Kong SAR, China.

### S1. IDENTIFICATION OF PHYSICAL PARAMETERS

#### A. Moment of Inertia

The inclusion of several components and manufacturing imperfection render it difficult to accurately estimate the moment of inertia of the robot from CAD software. Instead, this was experimentally measured using a customized setup shown in Fig. S1. The setup consists of two low-friction pulleys. The robot was fixated on the horizontal platform above one of the rotating pulley with the axis of rotation passing through the robot's center of mass. A cable originated from the base of the pulley was connected to a counterweight (80 g) via the second pulley, relating the rotation of the robot to the vertical displacement of the counterweight. The setup essentially converts the potential energy of the mass cube into the kinetic energy of both the weight to the rotational kinetic energy of the robot. Thanks to the use of low-friction bearings, the viscous loss was negligible.

To determine the moment of inertia of the robot along the axis of interest  $I_r$ , we let  $m_c$  be the mass of the counterweight,  $I_p$  be the lumped inertia of the entire platform, and  $r_p$  be the radius of the first pulley (where the cable was (see Fig. S1). Starting from a stationary state, the conservation of energy states that

$$\frac{1}{2}(I_p + I_r)\dot{\theta}_p^2 + \frac{1}{2}m_c r_p^2 \dot{\theta}_p^2 = m_c g r_p \theta_p, \quad (\text{S1})$$

where  $\theta_p$  is the angular displacement of the pulley (such that  $r_p \dot{\theta}_p$  is the vertical displacement of the counterweight). From here, the sum of the moments of inertia can be computed from the measurements of  $\dot{\theta}_p$  and  $\theta_p$  (via the motion capture system) taken at time  $t_i, t_f > 0$  as

$$I_p + I_r = \frac{2m_c g r_p (\theta_p|_{t_f} - \theta_p|_{t_i})}{(\dot{\theta}_p^2|_{t_f} - \dot{\theta}_p^2|_{t_i})} - m_c r_p^2. \quad (\text{S2})$$

First, performed the experiment without the robot to determine the inertia of the platform ( $I_r = 0$ ). In each trials, we recorded the displacement of the mass and the angular velocity  $\dot{\theta}_p$  at four timestamps (including the beginning). This created two pairs of  $(t_i, t_f)$  for the calculation of  $I_p$  as listed in Table S1. The experiment was repeated, resulting in four measurements of  $I_p$  in total. On average, we obtain  $I_p = 1.23 \text{ kg}\cdot\text{cm}^2$ .

The same procedure was repeated with the robot mounted on the platform in three different directions. This effectively allows us to compute the combined inertia about three primary axes as displayed in Table S1. According to the outcomes, we

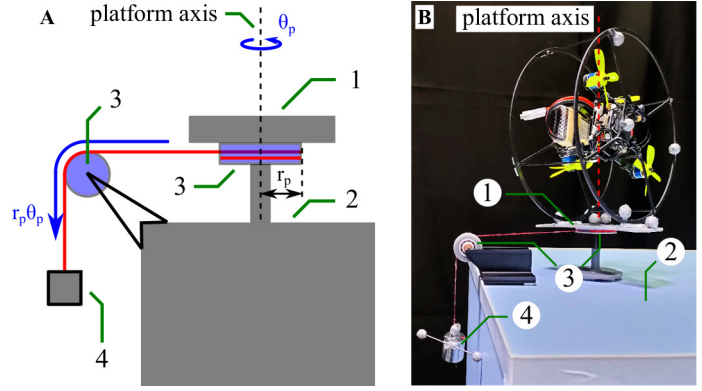


Fig. S1. Experimental platform for measuring the moments of inertia. The important elements are 1) a spinning platform; 2) the test bench; 3) pulleys; and 4) a counterweight. (A) A diagram showing major components of the platform and the parameters. (B) Photograph of the platform with the robot mounted. Markers are for the motion capture system for the measurements of  $\dot{\theta}_p$  and the displacement of the hung mass.

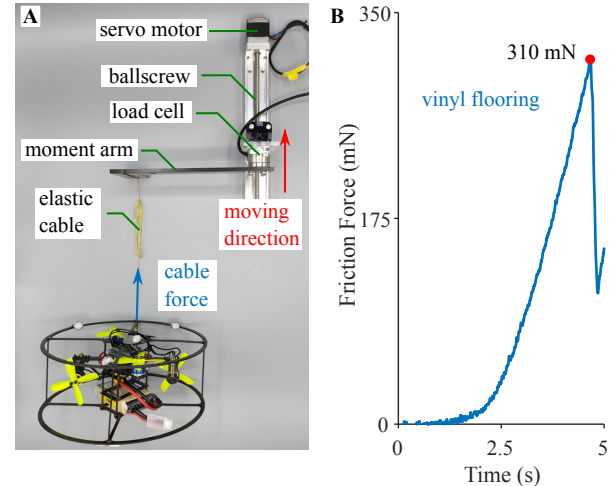


Fig. S2. (A) Test bench for the measurement of the coefficient of friction. (B) Static friction measurement result on vinyl flooring with peak value 310mN which is equivalent with the gravity of 31.6g weight.

obtain the averaged moments of inertia  $I_{X_B} = 1.98$ ,  $I_{Y_B} = 2.21$ , and  $I_{Z_B} = 2.42 \text{ kg}\cdot\text{cm}^2$  after subtracting out  $I_p$ .

These quantities are summarized in Table S3 and used for the numerical simulation for the roll-to-fly transition as described in the manuscript.

TABLE S1  
INERTIA MEASUREMENT RESULT

Parameter		Time Stamp		Inertia
		$t_i$ (s)	$t_f$ (s)	(kg·cm <sup>2</sup> )
$I_p$	1	0.00	0.15	1.25
		0.25	0.35	1.20
$I_p + I_X$	2	0.00	0.10	1.21
		0.20	0.30	1.27
$I_p + I_Y$	1	0.00	0.10	3.18
		0.20	0.35	3.23
$I_p + I_Z$	2	0.00	0.10	3.21
		0.20	0.30	3.23
$I_X$	1	0.00	0.10	3.46
		0.20	0.30	3.47
$I_Y$	2	0.00	0.10	3.44
		0.20	0.35	3.48
$I_Z$	1	0.00	0.20	3.71
		0.50	0.70	3.74
$I_Z$	2	0.00	0.15	3.57
		0.25	0.50	3.60

### B. Coefficients of Static Friction

To measure the coefficients of static friction between the robot and three ground surfaces (vinyl flooring, plywood, and EVA foam), a test platform presented in Fig. S2 was constructed from a load cell (ATI, Nano 25) mounted on a linear motorized stage. The setup was used to measure the pulling force required for the robot to start sliding on the surface.

To carry out the measurements, the robot is connected to the load cell via an elastic cable and a moment arm. The sensor was fixed on the linear motorized platform. Upon actuating the platform, the cable pulls the robot at the increasing force until it overcomes the static friction and the robot slides on the surface. The elastic cable was adopted to smoothen the pulling force and mechanically filter out the vibration of the motorized stage. The moment arm (with several cable mounting points) was used for (i) amplifying the force for the torque measurement and (ii) aligning the direction of the cable with the measurement axis of the load cell.

The tests were conducted with four different conditions: vinyl flooring, plywood (along and against the wood fiber direction), and EVA foam. Two measurements were performed for each condition. The measurement results are summarized in Table. S2.

### S2. ROLLING SPEED TEST

To quickly evaluate the rolling performance or the rolling speed, we commanded the robot to roll over the distance of 20 m (indoor) using the scheme outlined by Eq. 12. A constant command  $T_r$  was used.

During the test, the rotational rate about the axis  $Z_B$  or  $\omega_z^B$  was logged. The robot traveled the entire length of 20 m in less than 10 s. The instantaneous linear velocity is calculated

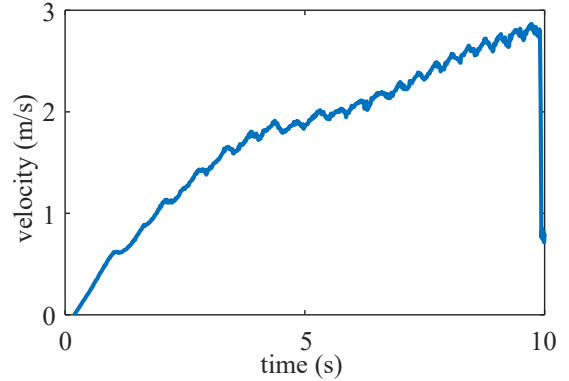


Fig. S3. Rolling velocity recorded during a 20-m terrestrial locomotion.

TABLE S2  
MEASUREMENTS OF THE COEFFICIENTS OF STATIC FRICTION.

Surface	Measured $\mu_s$	Average $\mu_s$
Vinyl flooring	0.21	0.22
Plywood (along the fiber)	0.38	0.39
Plywood (against the fiber)	0.61	0.61
EVA foam	0.76	0.77

as  $\omega_z^B r$  and the result is shown in Fig. S3. It can be seen that the robot was still accelerating throughout, with the velocity reaching up to 2.8 m/s (15.6 body lengths per second) towards the end. Note that the fluctuation in the speed reflecting the cyclic rotation is likely due to the cage being not perfectly rounded.

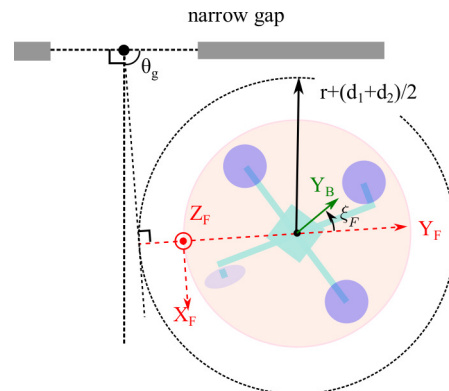


Fig. S4. Schematic diagram illustrating the process of passing through the gap. With the knowledge of the relative position of the gap's center and the center of mass, a tangent line is drawn from the gap's center to a perimeter of circle with radius  $r + (d_1 + d_2)/2$  from the center of the robot. The flipping direction  $\xi_F$  is determined from the robot's relative yaw angle. The through angle  $\theta_g$  depends on the position of center of mass and it is preferred to be close to  $90^\circ$ .

TABLE S3  
PARAMETERS IN THE ROLL-TO-FLY TRANSITION SIMULATION.

Item	Description	Value	Unit
$m$	mass of the robot	156	g
$I_X$	robot moment of inertia along $X_B$ axis	1.98	kg·cm <sup>2</sup>
$I_Y$	robot moment of inertia along $Y_B$ axis	2.21	kg·cm <sup>2</sup>
$I_Z$	robot moment of inertia along $Z_B$ axis	2.42	kg·cm <sup>2</sup>
$c_\tau$	propeller's thrust to torque coefficient	1.6	cm
$r$	radius of the wheel-like frame	9.0	cm
$r_m$	distance from the propeller to $Z_B$	5.4	cm
$d_1$	distance from the center of mass to the upper face	4.5	cm
$d_2$	distance from the center of mass to the lower face	3.0	cm

TABLE S4  
TABLE OF MULTIMEDIA EXTENSIONS.

Associated Files	Description	Type & Format	Size (MB)
S1_quadrotor_hybrid_locomotion.mp4	Video of the quadrotor with hybrid locomotion trajectory and the transitions between two locomotion modes	Video/MP4	34.8